

## **NOTICE CONCERNING COPYRIGHT RESTRICTIONS**

This document may contain copyrighted materials. These materials have been made available for use in research, teaching, and private study, but may not be used for any commercial purpose. Users may not otherwise copy, reproduce, retransmit, distribute, publish, commercially exploit or otherwise transfer any material.

The copyright law of the United States (Title 17, United States Code) governs the making of photocopies or other reproductions of copyrighted material.

Under certain conditions specified in the law, libraries and archives are authorized to furnish a photocopy or other reproduction. One of these specific conditions is that the photocopy or reproduction is not to be "used for any purpose other than private study, scholarship, or research." If a user makes a request for, or later uses, a photocopy or reproduction for purposes in excess of "fair use," that user may be liable for copyright infringement.

This institution reserves the right to refuse to accept a copying order if, in its judgment, fulfillment of the order would involve violation of copyright law.

# Modeling of Surface Deformation from Satellite Radar Interferometry in the Salton Sea Geothermal Field, California

Mariana Eneva and David Adams

Imageair, Inc., San Diego, CA  
[meneva@imageair-inc.com](mailto:meneva@imageair-inc.com)

## Keywords

*Geothermal, Salton Sea, Imperial Valley, PSInSAR, permanent scatterers, radar interferometry, surface deformation, subsidence*

## ABSTRACT

Surface deformation in the Salton Sea geothermal field is modeled using results from satellite radar interferometry, data from leveling surveys, and observations from the regional GPS network. The field is located in the Salton Trough, an active spreading center in southern California, which is traversed by the Brawley seismic zone. Deformation time series at thousands of points in the study area are obtained from a PSInSAR™ (permanent scatterers interferometric synthetic aperture radar) analysis of two-year Radarsat satellite data covering the period May 2006 - March 2008. SAR scenes from two orbit geometries are used, descending and ascending, which makes it possible to convert the deformation rates obtained in the line-of-sight (LOS) to the satellite, into vertical and horizontal components. These are further interpolated to model the surface deformation rates throughout the field. The results are constrained with ground-based leveling observations. Two main subsidence areas are observed in the geothermal field, with maximum vertical and horizontal deformation rates of up to 30 mm/year, relative to a reference point on Obsidian Butte, less than 5 km away. Comparisons are also made with the time series of production and injection fluid, as well as with seismicity. No simple spatial connection between the areas of maximum subsidence, locations of wells, and seismicity is found. It is estimated that the regional tectonic contribution to the maximum deformation rates in the field is at most 10%. The remainder may be accommodated to a large extent by the local tectonics, as there are arguments that the geothermal operations do not contribute significantly to surface deformation. In the absence of surface expression of faults in the study area, these effects cannot be properly estimated at this time. An ongoing analysis of seismicity is intended to partially address this uncertainty.

## Background

The results discussed in this paper represent a continuation of a work previously reported by Eneva et al. (2009). In that study, an InSAR (interferometric synthetic aperture radar) approach based on so-called “permanent”, or “persistent,” scatterers (PS) was used to extract surface deformation time series at numerous PS points on the territory of the Salton Sea geothermal field (Figure 1). This type of techniques is also known under the general name of PSI (permanent or persistent scatterers interferometry). The specific PSI technique used by Eneva et al. (2009) was

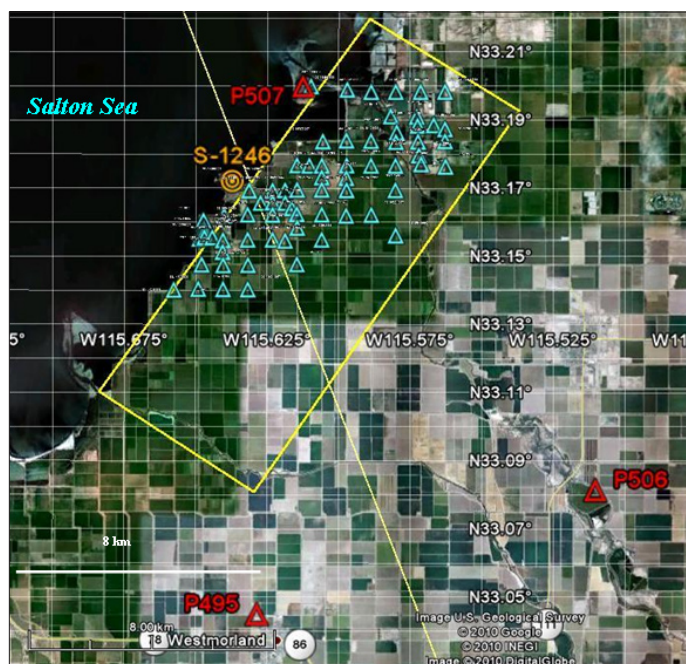


**Figure 1.** Map of the Salton Sea geothermal field and surrounding area. Study area is marked with yellow rectangle. Locations of leveling benchmarks are shown with blue triangles. Locations of stations from the PBO GPS network are marked with red triangles. Location of the reference leveling benchmark, S-1246, is shown with orange circle. (Superimposed on a Google Earth image).

PSInSAR<sup>TM</sup> (permanent scatterers InSAR), as described by Ferretti et al. (2000, 2007). The data used were synthetic aperture radar (SAR) scenes from the Canadian satellite Radarsat. They covered a nearly two-year period, May 2006 – March 2008. The PS points represent objects with sub-pixel size on the SAR images, which remain coherent from one scene to another, so that time series of deformation can be extracted at their locations. They are positioned on buildings, roads, large boulders, and the like. The PS points can be thought of as numerous tiny benchmarks covering the study area. The SAR data were collected from descending and ascending orbits, i.e., when the satellite moved north-south and south-north, respectively. The availability of 21 descending and 18 ascending SAR scenes over the study area made it possible to combine the results from these different geometries for the purpose of converting the deformation observed in the line-of-sight (LOS) direction to the satellite into two components – a vertical component and a horizontal component in the west-east direction. The two orbit geometries are such that the horizontal component in the south-north direction cannot be constrained. Still, it is a great advantage to be able to decompose the results in at least two components, because the information from the LOS deformation is limited only to determining if surface movement has occurred towards the satellite or away from it.

The PSInSAR<sup>TM</sup> technique used by Eneva et al. (2009) and described in detail by Ferretti et al. (2000, 2007), is an extrapolation of earlier InSAR techniques, which only worked in relatively dry areas. Conventional approaches do not yield any results in vegetated areas, especially such as the territory of the Salton Sea geothermal field, which is extensively covered by agricultural lands. Thus without PSInSAR, satellite interferometry is completely ineffective for detecting ongoing surface deformation in the study area. In the case of the Radarsat SAR data used for the Salton Sea geothermal field, more than 4,000 PS points were identified within the study area from the descending scenes and more than 3,000 PS points from the ascending scenes. They are generally aligned along roads and canals – see Figure 3 in Eneva et al. (2009). The LOS deformation rates were determined from the descending and ascending deformation time series at the PS points, in terms of average deformation per year. The study area was then split into cells of size 50 m x 50 m, and for all cells in which there were PS points of both the descending and ascending type, the mean vertical and W-E horizontal components were calculated – see Figure 5 in Eneva et al. (2009). However, this procedure left out a large portion of the study area, covered by cells in which there were no PS points at all, or there were only PS points from one type (i.e., either only descending, or only ascending). The deformation modeling presented here interpolates between the PS points and results in a smoothed and continuous image of surface deformation in the Salton Sea geothermal field. Thus the analysis here yields a more advanced interpretation of the PSInSAR results, compared with the one reported by Eneva et al. (2009) in terms of individual small cells with deformation rates.

CalEnergy, the operator of the Salton Sea geothermal field, has provided annual leveling data collected at 79 benchmarks. These benchmarks cover only about half of the study area (Figure 1), so the use of satellite data has the obvious advantage of covering larger areas than those in covered by the leveling surveys. Also, the repeated temporal coverage by the satellite is much more frequent

than the annual leveling surveys – for the study period between May 2006 and March 2008, 21 descending and 18 ascending Radarsat scenes became available for PSInSAR analysis, while only two leveling surveys were carried out. Nonetheless, the leveling data provide an important baseline, to which the satellite results were compared. Eneva et al. (2009) showed examples of excellent agreement between the deformation measured by leveling (vertical movements) and the satellite results.

The leveling data provided by CalEnergy are referenced to one of the benchmarks, S-1246, located on Obsidian Butte (Figure 1). All satellite results reported by Eneva et al. (2009) and in this paper are also referenced to this point, as if it is motionless. However, there are GPS stations from the Plate Boundary Observatory (PBO) network in the region, the closest three of which are shown in Figure 1. Unlike leveling benchmarks, GPS stations provide information on all three components of surface deformation - vertical, west-east (W-E), and south-north (S-N). One of the GPS stations, P507, is located close to one of the CalEnergy's leveling benchmarks on Red Island. Comparing the vertical component recorded at P507 and the leveling measurements, made it possible to establish that S-1246 actually moves, and that what looked as an uplift of Red Island compared to S-1246, was in fact just a slower subsidence than that of S-1246 (Eneva et al., 2009). This comparison made it possible to estimate that S-1246 likely subsides at a rate of 18 mm/year. Nonetheless, for the sake of consistency, all further discussions of surface deformation are in relation to S-1246.

The Salton Trough is a spreading center characterized by active tectonics (e.g., Hill, 1977), so it is to be expected that both subsidence and horizontal movements take place on a regional scale. This is confirmed by the observations at the GPS stations in the region that are mostly outside of the Salton Sea geothermal field, except for P507 on its edge – see Eneva et al. (2009) for a list of rates at GPS stations surrounding the field. Also, subsidence of 30 to 40 mm/year was reported by Lofgren (1979) based on leveling surveys in the 1970's, before the geothermal field development. The reference point in that case, was a benchmark near the U.S. – Mexico border, 50 km southwest from El Centro. In addition, there may be movements due to local tectonics in the study area, such as that of blocks formed by a network of faults, of both strike-slip and normal type. There is no obvious surface expression of faults in the study area; that is, such faults may be blind (i.e., not reaching the surface) and/or obscured by the agricultural fields. The observations at the GPS stations from the PBO network and Lofgren's (1979) surveys cannot help in this respect either, because they are too coarse to reflect movements on local structures in the study area. Therefore, it is difficult to evaluate the possible contribution of local tectonics. Nonetheless, it is likely significant, especially in light of recent studies (Brothers et al., 2009) just north of the study area, using seismic reflection data collected from the Salton Sea. These authors note that oblique extension across strike-slip faults causes subsidence, leading to the formation of pull-apart basins, such as the Salton Sea and surrounding areas. They project maximum subsidence near the southern shoreline of the sea, approximately coincident with the locations of Quaternary volcanism and a northeast-trending band of very high heat flow, located within the study area in this paper (Figure 1).

In addition to the relatively gradual deformation due to regional and local tectonics, the Salton Trough has experienced abrupt surface ruptures due to larger earthquakes and associated aseismic slip (e.g., Fay and Humphreys, 2005; Genrich, 1997). Brothers et al. (2009) have interpreted seismic reflection data from the Salton Sea to indicate that relatively infrequent, but larger earthquakes ( $M > 6$ ) accommodate extension and subsidence, whereas the smaller events ( $M < 5$ ) and microseismicity in the BSZ are due to fracturing and block rotation within narrow ( $< 5$ -km-wide), dextral shear zones. Within this framework, the territory of the Salton Sea geothermal field has seen its share of seismic swarms and accompanying aseismic slip, the most recent ones in 1981, 1989, and 2005. A broad zone, so-called Brawley Seismic Zone (BSZ), represents the transitional zone between the southern tip of the San Andreas fault to the northeast, and the Imperial fault to the south of the Salton Sea. It traverses the Salton Sea geothermal field, without being associated with faults with surface expressions in the study area. However, an InSAR application to two descending SAR images from the European satellite Envisat, collected 35 days apart before and after the M5.1 earthquake in September 2005, detected a 14-cm surface deformation in the LOS direction (Lohman and McGuire, 2007). Since the M5.1 main shock and its foreshocks and aftershocks, which occurred mostly between the end of August and the end of December 2005, could not accommodate such a large displacement, the authors attributed about 80% of it to aseismic slip accompanying the swarm.

Eneva et al. (2009) already reported that the PSInSAR results from the Salton Sea geothermal field indicate maximum subsidence (relative to S-1246) of about 30 mm/year at two main locations. The horizontal eastward movement (also relative to S-1246) reaches 30 mm/year as well. Note that the similar rate of subsidence reported by Lofgren (1979) is over a distance of about 70 km (between the U.S. – Mexican border and the Salton Sea shore), whereas the PSInSAR results here refer to not more than 5 km distance between the sites of maximum subsidence at the Salton Sea geothermal field and S-1246. Thus the PSInSAR observations of the two subsidence bowls are essentially superimposed on the ongoing regional subsidence.

## Deformation Modeling

Linear interpolation was applied to the point observations reported earlier by Eneva et al. (2009). Figure 2 shows the results for the vertical deformation in cells of size 200 m x 200 m. The panel on the right of this figure shows the individual descending PS points, at which the deformation time series were used to evaluate vertical deformation rates. The ascending PS points (not shown) are distinct and generally different, although they too align mostly along the same roads and canals. Figure 2 displays two obvious subsidence bowls, with apparent elliptical shapes, of size  $\sim 5.8$  km x 4.6 km and  $\sim 6.9$  km x 5.8 km. They are located to the west and to the east of a relatively arbitrary line, which does not represent

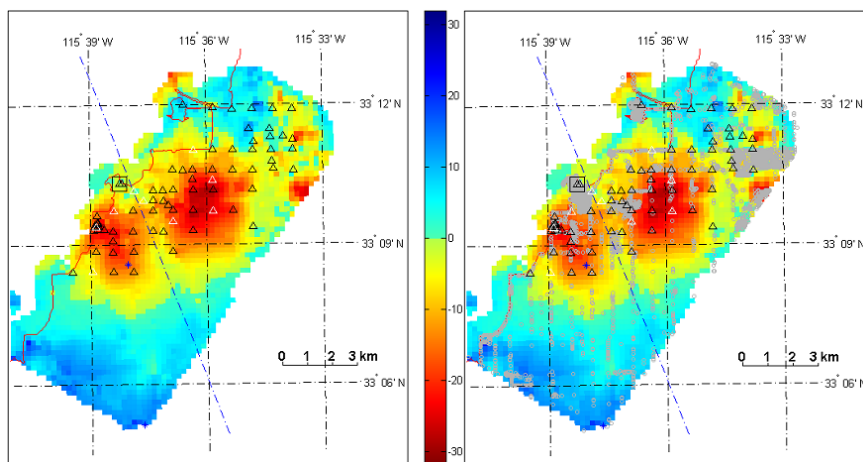


**Figure 2.** Vertical rates of surface deformation at the Salton Sea geothermal field from PSInSAR™ analysis of Radarsat-1 data for the period May 20, 2006 – March 27, 2008. Square shows location of a reference benchmark, S-1246, on Obsidian Butte. Rates are linearly interpolated from the deformation rates at individual PS (permanent scatterers) locations for the descending and ascending orbits. Warm colors (yellow to red) indicate subsidence, and cold colors (light to dark blue) show uplift, both in relation to S-1246. These are represented by the vertical color bar between the two plots showing surface deformation in mm/year. Red outline shows the Salton Sea shore. Dashed blue line across the field marks an arbitrary line (from a USGS fault data set) around the middle of the broad Brawley Seismic Zone traversing the field. Black triangles show locations of benchmarks, for which leveling data exist before, during, and after the study period; white triangles mark benchmarks with data only prior to the study period. Left – surface deformation in 200 m x 200 m cells. Right – same as plot on the left, but showing superimposed the locations of the individual descending PS points (grey circles) used in the interpolation.

a known fault, but just the middle of the BSZ (fault data from the California Geological Survey and USGS – Bryant, 2005).

The left panel of Figure 3 zooms in on Figure 2 and shows in enlarged plan the subsidence bowls on the background of the vertical movements measured by PSInSAR. The same area is shown also in the panel to the right, but with the horizontal W-E (west-east) movements; as a reminder, the horizontal S-N (south-north) component cannot be deduced from the PSInSAR observations. The ellipses in Figure 3 outline the apparent areas of larger subsidence. The “drag,” or “pull” of the subsidence is expected to lead to horizontal movements towards the inner parts of the subsidence bowls. Since horizontal displacements are in the opposite directions at the opposing sides of the bowls, they cancel each other somewhere within them. The right panel of Figure 3, showing the W-E component of the horizontal movements, demonstrates the interplay between vertical and horizontal displacements. The smaller subsidence bowl is distinctly split almost in the middle by eastward horizontal movements in its western portion and westward movements in its eastern portion, as it would be expected from the observed subsidence. The larger subsidence bowl also displays a pattern of eastward and westward horizontal movements, although their spatial configuration is tilted compared with the smaller bowl. To clarify the vertical and W-E horizontal components of surface displacement, the deformation rates along two profiles are also shown in Figure 3, beneath the maps showing the vertical and west-east components. The longer profile (AA') traverses both subsidence bowls, while the shorter profile (BB') captures opposing horizontal movements in the larger subsidence bowl. These profiles clearly illustrate that subsidence of up to 30 mm/year is observed in the larger bowl, and that the

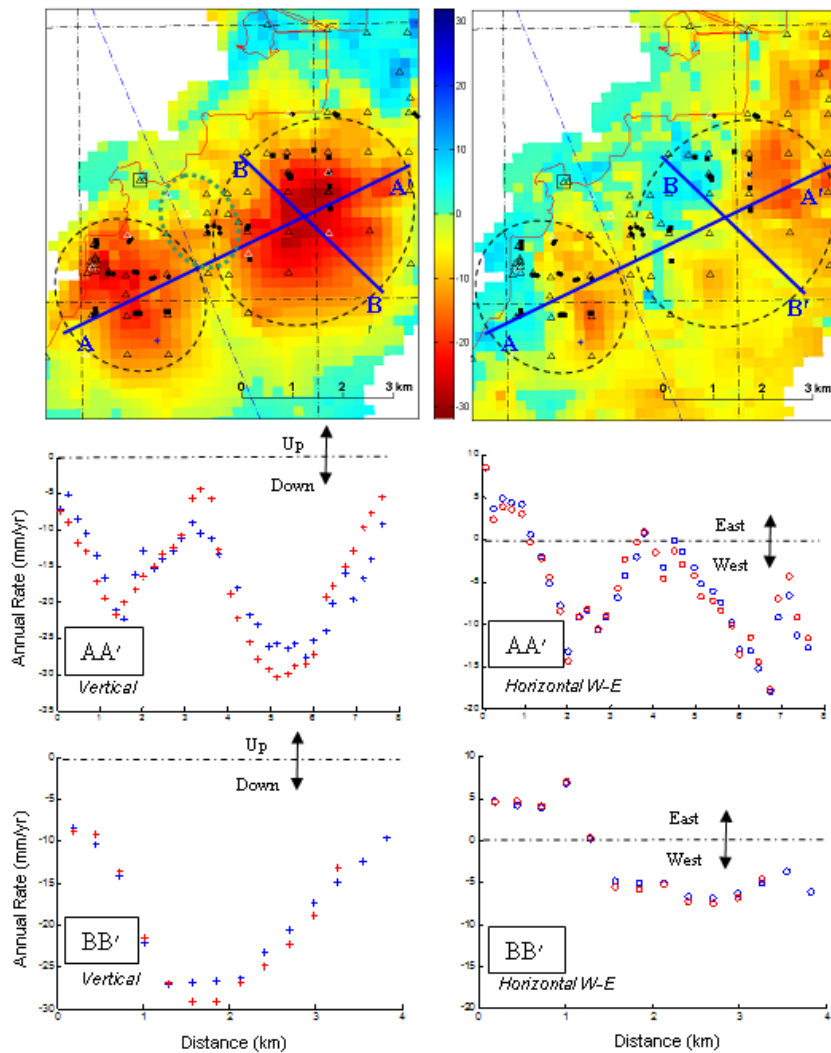


**Figure 3.** Examples of deformation profiles. Left – vertical rates. Right – horizontal west-east rates. Maps on top – in the plot on the left yellow to red colors indicate subsidence and blue colors mark uplift; in the plot on the right yellow to red colors indicate westward horizontal movement and blue colors show eastward movements. Black outlines mark the two subsidence bowls. Green outline is discussed further in connection to Figure 4. Black circles and squares show locations of production and injection wells, respectively. Blue lines denote profiles AA' and BB', along which deformations rates are shown beneath the maps. Remaining notations as in Figure 2. Four plots under maps - crosses and circles show vertical and horizontal west-east rates, respectively, along profiles AA' (middle) and BB' (bottom). Red symbols show interpolation using only satellite data. Blue symbols show interpolation using both satellite and ground-based leveling data.

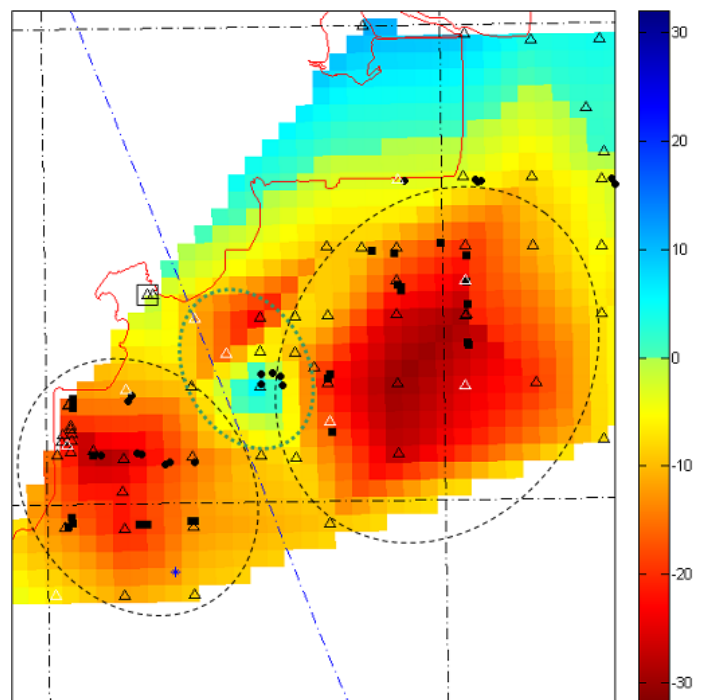
the leveling measurements. The obvious difference is due to a single benchmark that shows uplift (relative to S-1246). Since PS points are lacking in the immediate area of this benchmark, this apparent localized uplift is missed by the PSInSAR analysis. Alternatively, this particular benchmark could have wrong measurements. Nonetheless, this illustrates that although many PS points are positioned in parts of the study area where there are no leveling benchmarks, thus providing unique information on surface deformation, there are some locations where there are benchmarks, but no PS points. In a future satellite monitoring, it will be possible to remedy such a situation by installing reflectors to assure the identification of PS points in strategic locations in future SAR imagery.

Furthermore, it is possible to do a detailed analysis of small subareas of the study area. Figure 5 shows examples, where two subareas contain some benchmarks and injection and production wells. The various panels

maximum horizontal westward component in it approaches 20 mm/year. The horizontal eastward component generally reaches ~ 5 mm/year. The asymmetry between the westward and eastward movements may be partially due to the movement of the reference point (S-1246) in south-southeast direction.

The deformation profiles shown in Figure 3 are of two types. The first type is calculated only from the satellite data and the overall results are the ones shown in the maps on the top of Figure 3. The second type is based on the satellite results as well, but is additionally constrained by the ground-based leveling data provided by CalEnergy. Reassuringly, there is not much of a difference between the two types of estimates of the horizontal W-E components, over most of the study. However, there is an area with a significant difference between the vertical movements calculated with the two approaches. It is marked with a small green ellipse in the left map panel of Figure 3 (vertical movements calculated only from the satellite data) and Figure 4, which shows a map of the vertical movements calculated from both the satellite data and

**Figure 4.** Vertical deformation rates interpolated from satellite observations and leveling measurements. Area outlined with green dashed ellipse shows differences compared with interpolation deformation rates based only on satellite data (upper left plot in Figure 3). Other notations as in Figures 2 and 3.



in this figure show total monthly production and injection, monthly production and injection for individual wells, vertical and W-E deformation time series in the individual 200 m x 200 m cells within the two subareas and their means for the whole subareas, deformation time series from the leveling data, and times of earthquake occurrences. The zero of the deformation time series on the vertical axes starts on May 20, 2006, which is the beginning of the available Radarsat SAR data, so this date also marks zero days on the horizontal axes. The satellite data used in this study start about five months after the end of the M5.1 swarm in the fall of 2005. There were no earthquakes in these small subareas for the period covered by the SAR data, but earthquakes

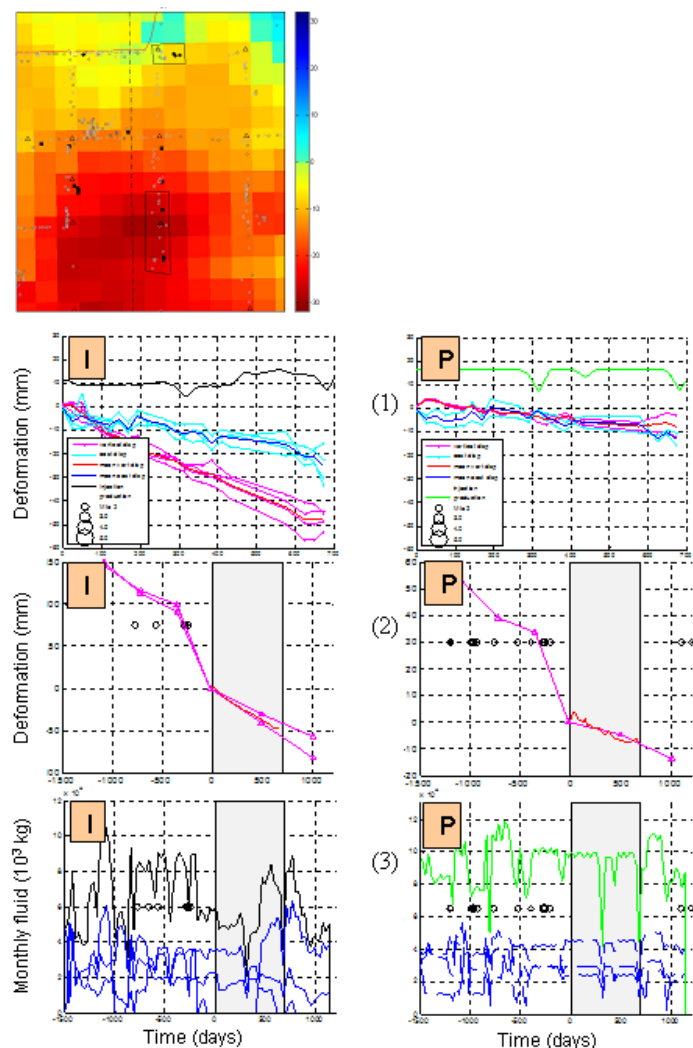


**Figure 5.** Examples of deformation time series from small subareas with injection (I) and production (P) wells. Map zooms in on Figure 2 and upper left of Figure 3. From top to bottom: (1) Vertical deformation time series from PSInSAR, May 2006 – March 2008, at individual 200 m x 200 m cells (pink) and their means (red); same for horizontal W-E deformation (light and darker blue); total monthly fluid (black curve for injection, green curve for production); (2) Leveling deformation time series (pink lines and triangles), May 2003 – May 2009; grey rectangle marks period of satellite data; red curve shows mean of vertical deformation from PSInSAR (same as red curve in (1)); circles denote times of earthquakes within subareas I and P; (3) Total monthly fluid (like in (2)) - black curve for injection, green curve for production) and at individual wells (solid blue curves for injection and dashed blue curves for production); remaining notations like in (2).

occurred before and after that, some of which are 2005 aftershocks. Another observation is that at least in these examples, there are rather small vertical and horizontal movements over the subarea with the production wells. The subarea with the injection wells happens to be near the largest observed subsidence and relatively significant westward horizontal movements. Note that good agreement is observed between the vertical movements measured from PSInSAR and the leveling data. No obvious association is seen between the occurrence times of earthquakes and monthly production or injection. If anything, significantly reduced production and absence of earthquakes coincide during the first half of the study period, which may be associated with the post-seismic effect of the 2005 M5.1 swarm.

## Effect of Regional Tectonics

In an attempt to evaluate what portion of the surface deformation observed with PSInSAR may be explained by regional tectonics, GPS data were used to evaluate movements relative to S-1246. Figure 6 shows a simple linear model using GPS measurements from the larger vicinity of the Salton Sea geothermal field. GPS data were acquired from the Scripps Orbit and Permanent Array Center (<http://sopac.ucsd.edu/>). Examining the modeled vertical and horizontal movements within the study area, it is noticed that the largest subsidence is around P507 and is about 3 mm/year (relative to S-1246). The regional tectonic subsidence at the locations of maximum observed vertical deformation in the two subsidence bowls is even smaller than that – at most 1.5 mm/year uplift in the smaller bowl to the west (i.e., in the opposite direction of the subsidence), and at most 1.5 mm/year subsidence in the larger

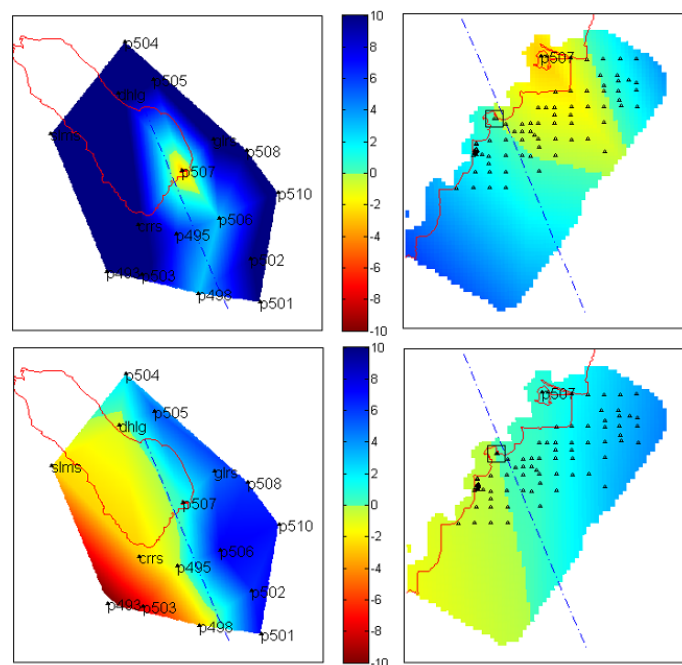


**Figure 6.** Model of regional tectonic effect based on GPS measurements. Labels with letters and digits show GPS stations. Left – larger region around the Salton Sea geothermal field. Red outline marks the Salton Sea shore. Right – study area (as in Figs. 2 and 3). Top – regional tectonic vertical deformation rates. Bottom – regional horizontal W-E deformation rates. Color bar shows deformation in mm/year. Other notations like in Figure 2.

bowl to the east. The largest uplift in the study area is up to 5.6 mm/year in the western part and 4 mm/year in the eastern part of the study area. Compared with the maximum observed subsidence from PSInSAR of 30 mm/year, not more than 5% of the subsidence in the larger subsidence bowl can be accommodated by regional tectonic movements. Even if the maximum modeled tectonic subsidence around P507 is taken for this estimate (although it is outside the larger subsidence bowl), only up to 10% of the observed subsidence can be explained by regional tectonics.

Similar considerations for the horizontal W-E components show maximum horizontal movements within the limits of the subsidence bowls, modeled from regional tectonics, to be a negligible  $\sim 0.3$  mm/year westward in the smaller subsidence bowl, and  $\sim 2$  mm/year eastward in the larger subsidence bowl. This means that where westward movement is observed from PSInSAR in the smaller subsidence bowl (i.e., up to 15 mm/year), not more than 2% can be accommodated by regional tectonic movements. Where eastward movements are observed (up to 5 mm/year), they might have been about 6% larger if it were not for the regional tectonic movement pulling in the opposite direction. Because eastward movements from PSInSAR are quite smaller ( $\sim 5$  mm/year) than the westward ones, up to 40% of the eastward deformation in the larger subsidence bowl may be accommodated by regional tectonics. However, the larger PSInSAR horizontal components are westward (up to 18 mm/year), which is in the opposite direction of the regional tectonics in the larger subsidence bowl. Thus without the regional horizontal movement pulling in the opposite direction, the PSInSAR observations might have been about 10% larger.

These constrains show that while regional tectonics may explain small deformation values in some locations of the study area, it explains at most only 10% of the larger surface deformation in and around the subsidence bowls. That is, the contribution of regional tectonics to the maximum localized movements observed with PSInSAR is relatively small.

## Effect of Local Tectonics

The effect of local tectonics on the territory of the Salton Sea geothermal field may be significantly larger than that of regional tectonics. It could be related to gradual and episodic aseismic slip on faults in the local area, as well as abrupt changes due to earthquakes. Aseismic slip may accompany larger earthquakes or it may occur at times without seismic activity. To properly evaluate the possible local effect, a detailed knowledge of faults in the study area is needed, which is lacking at this time. Thus it is not known if all of the remaining 90% (or more) of the observed surface deformation can be accommodated by local tectonic movements, given that the effect of regional tectonics is relatively small and likely does not extend to more than 10% at the locations of largest surface deformation. Surface expressions of faults on the territory of the Salton Sea geothermal field are absent, either because the faults are blind or because they are concealed by the agricultural fields. However, extrapolating from faults in the outer region, and recent analysis by Brothers et al. (2009), it is logical to assume that there may be dextral strike-slip faults in the study area, oriented southeast-northwest, as well as normal faults, oriented southwest-northeast. At present, the locations of earthquake hypocenters and

their fault mechanisms represent the only source of information about possible faults in the study area.

To put seismicity in the study area in perspective, it is to be noted that a number of  $M \geq 5.5$  earthquakes have occurred in the Salton Trough in the 20<sup>th</sup> century, with most seismic release on the Imperial Fault (e.g., Genrich et al., 1997). The Brawley Seismic Zone (BSZ), which traverses the territory of the Salton Sea geothermal field, is the main transfer zone between the Imperial fault and the southern tip of the San Andres fault, which is considered to be ripe for a large earthquake (e.g., Fialko, 2006). Most of this transition zone is represented by a broad area, without much surface expression, but marked by numerous small and some moderate earthquakes, many of them in swarms (e.g., in 1981, 2005, 2009). Lohman and McGuire (2007) suggested that these swarms are associated with significant aseismic creep, possibly connected to the extensional tectonic setting of the Salton Trough driven by magmatic intrusions (Hill, 1977) and the effects of high geothermal gradients (Ben-Zion and Lyakhovskiy, 2006). Unlike the part of the BSZ around the Salton Sea shore, the southern part of the BSZ is more clearly expressed on the surface as the Brawley fault, near the Imperial fault. Two large earthquakes that occurred on the Imperial fault, M7.1 in 1940 and M6.9 in 1979, caused surface ruptures also on the Brawley fault.

The Imperial fault accommodates close to 80% of the relative motion between the Pacific and North American plates, with average slip rates estimated at 15-20 mm/yr (Thomas and Rockwell, 1996) to 35-43 mm/yr from geodetic surveys (Lyons et al., 2002). Partitioning of the plate boundary deformation further north, between the San Andreas and San Jacinto faults, has been debated. The latest estimates from GPS indicate  $\sim 21$  mm/yr and  $\sim 15$  mm/yr, respectively (Fay and Humphreys, 2005) and from GPS/InSAR  $\sim 25$  mm/yr and 19 mm/yr (Fialko, 2006).

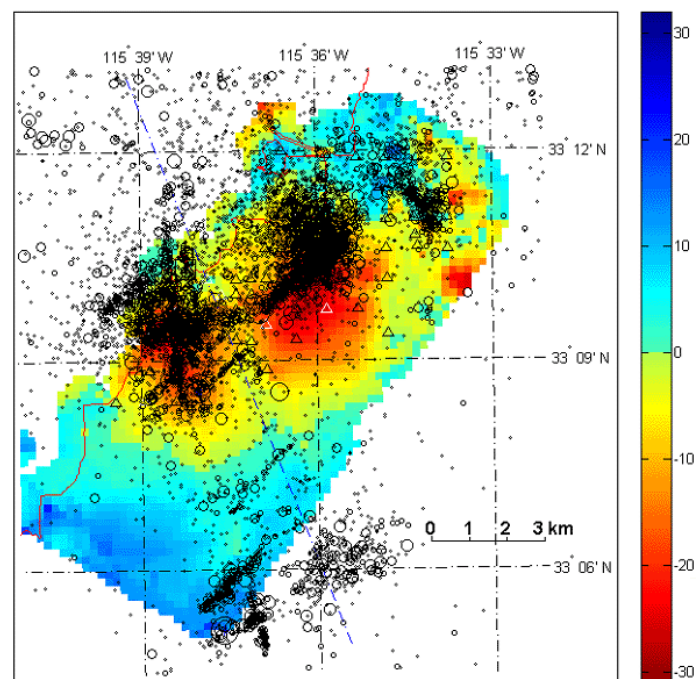


**Figure 7.** Earthquake epicenters (January 1981 – March, 2010) superimposed on vertical deformation rates from the PSInSAR observations (as in Figure 2). Circle size increases with magnitude.

What happens in between, however, at the BSZ transferring the strain, is not that clear, especially because paleoseismic studies measuring the vertical slip from earthquakes and aseismic creep indicate recent acceleration compared with the long-term trend (Meltzner et al., 2006).

Figure 7 shows a seismicity map using earthquake locations from two sources. The most accurate earthquake catalog for southern California has been provided by Lin et al. (2007) for the period 1981–2005. Earthquake locations after 2005 are from the Southern California Seismic Network (SCSN) catalog, which are less accurately located, especially at depth. The seismicity map in Figure 7 shows several main clusters that are mostly due to swarm activity in 1981 (in the southernmost part of the study area), 1989, and 2005. Note that the maps show epicentral locations, i.e., the surface projections of the earthquake hypocenters at depth. The hypocenters may be on fault planes that are not vertical and thus their projections on the surface can be shifted compared with surface features, such as those suggested by the subsidence bowls. The seismicity map displays a number of apparent linear features that may trace faults at depth. Many of these apparent seismic lineaments are with southwest-northeast orientation.

Figure 8 displays a seismicity map of the M5.1 swarm in 2005, which began at the end of August and continued until the end of December, about five months before the start of the study period in this paper. The relocated events (Lin et al., 2007) align very well on two linear features across the two subsidence bowls. They may represent events on the same fault plane striking southwest-northeast, with the apparent shift due to deeper hypocentral depths under the smaller subsidence bowl to the southwest compared to those under the larger subsidence bowl. Indeed, the right panel of Figure 8 showing a cross-section along the rectangle outlined on the seismicity map indicates that the hypocentral depths become shallower from southwest to northeast. The shift between the two linear features on the map may thus also indicate that the fault plane dips to the northwest. This analysis is in progress and will be further combined with examination of the fault-plane solutions of the seismic events, available for earthquakes with magnitudes  $M \geq 2.0$ .

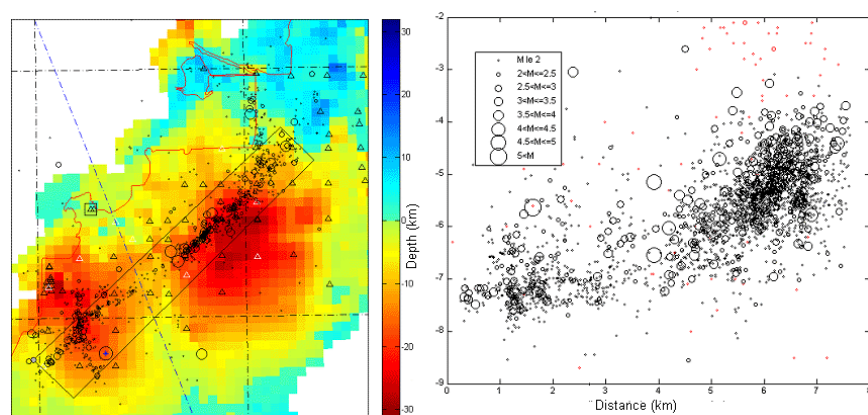


**Figure 8.** Earthquake epicenter map and depth distribution in the area of a September 2005 M5.1 earthquake. Left - Foreshocks and aftershock epicenters in the period August – December, 2005, superimposed on map of vertical deformation. Right – Depth cross-section of earthquakes in rectangle shown on the map. Black circles denote hypocenters of earthquakes in the period January 1981 - December 2005, relocated by Lin and Shearer (2007). Red circles show events occurring in the period January 2006 – March 2010, from the SCSN earthquake catalog.

## Other Effects

There could be additional reasons for the surface deformation observed in the Salton Sea geothermal field, most notable among them the geothermal operations. Subsidence associated with geothermal fields has been well documented elsewhere, including in studies applying conventional radar interferometry (e.g., Oppliger et al., 2006, 2008; Fialko and Simmons, 2000; Wicks et al., 2001). A subsidence as large as 16 cm/year has been observed with InSAR in the Cerro Prieto geothermal field in Mexico (Carnec and Fabriol, 1999; Hanssen, 2001), south of the Salton Sea geothermal field. In these studies, the geothermal operations are assumed to be the primary reason for the subsidence. However, the tectonic situation at the Salton Sea geothermal field is rather complicated and there is insufficient knowledge at present to ascertain if geothermal production contributes to the observed surface deformation or local tectonics is sufficient to accommodate it. The analysis carried out by Brothers et al. (2009) for the Salton Sea can be conceptually extended to the south, into the study area here, and thus substantial subsidence due to local tectonics is very likely. The following arguments that the influence of the geothermal operations must be minimal at the Salton Sea geothermal field have been presented (personal communication, Alex Schriener from CalEnergy): pressures and subsurface fluid level have changed very little for the 30 years of field operation; only a small portion of the vast total resource has been exploited so far; production wells are relatively deep (mostly between 600 m and 1,800 m, and in some places down to 2,700 m); and at least 75% of the produced fluid is re-injected at depths below 1,800 m. Information on reservoir pressure and temperature changes, as well as fault interpretation from well cores is proprietary, so modeling based on such parameters is not feasible at this time.

Since the Salton Sea geothermal field is covered by agricultural fields, another effect on surface deformation may be contributed by the different types of soils and the variable patterns of irrigation, causing various amounts of compaction and expansion. This is a subject of future analysis. However, this effect is likely secondary to local tectonics and geothermal operations, and due to the rotation of various crops and seasonal changes in irrigation, it is not expected to be associated with a long-term steady trend. Also, it would likely be associated with a checkered spatial pattern characteristic for the individual agricultural fields, rather than be spatially organized into the distinct subsidence bowls observed here. A seasonal variability was not captured in the two-year data in this study, but may be revealed if a period of longer duration is studied. There are no Radarsat data covering a longer period of time, however SAR scenes from the European satellite Envisat have been collected since 2003. This longer-term SAR imagery will be used in a future study.

## Conclusions

The PSInSAR analysis presented here was very effective in determining surface deformation in the area of the Salton Sea geothermal field. The pres-

ence of agricultural fields in the study area renders conventional satellite interferometry ineffective, so the PSInSAR technique is the only one that could yield results for this field. Since data from two orbit geometries were available, it was possible to deduce both vertical movements and the west-east component of the horizontal movements. Two distinct subsidence bowls were outlined, with subsidence rates of up to 30 mm/year relative to a reference point a short distance away on Obsidian Butte. The drag of the subsidence is associated with horizontal movements, whose west-east component could be also resolved and found to follow the expected spatial pattern.

The contribution of regional tectonics associated with the spreading at the Salton Trough, is relatively small, explaining at most 10% of the maximum surface deformation observed at the Salton Sea geothermal field. The degree to which local tectonics explains the remaining deformation is not known, due to lack of information on local faults. However, some inferences about possible fault planes can be deduced from the seismicity in the study area, using precise hypocentral locations and fault-plane mechanisms, which is a work in progress.

The above uncertainties emphasize the importance of establishing baseline deformation prior to the start of future geothermal operations. This will clarify in advance the effects of regional and local tectonics and their variability in time, so that there will be much less ambiguity in separating tectonic and man-made effects.

## Acknowledgments

This work has been funded by the Geothermal Resources Development Account (GRDA) program of the California Energy Commission (CEC). CalEnergy Generation is thanked for providing digital data from the annual leveling surveys at the Salton Sea geothermal field. Alex Schriener and Jon Trujillo from CalEnergy are thanked for numerous discussions and answering various questions. They also carefully reviewed this paper and provided valuable suggestions for improving it. Brian Berard from TerraGen Power (formerly with CalEnergy) helped significantly with the leveling data. Sabodh Garg from SAIC has participated in discussions about the causes of subsidence in geothermal fields. Gary Oppliger from Magma Energy Corporation is thanked for discussions related to InSAR applications in geothermal fields and their interpretation.

## References

- Ben-Zion, Y., and V. Lyakhovskiy, 2006. Analysis of aftershocks in a lithospheric model with seismogenic zone governed by damage rheology, *Geophys. J. Int.* 165, p. 197–210.
- Brothers, D.S., N.W. Driscoll, G.M. Kent, A.J. Harding, J.M. Babcock, and R.L. Baskin, 2009. *Nature Geoscience* 2, p. 581–584, doi: 10.1038/NCEO590.
- Bryant, W.A. (compiler), 2005. Digital Database of Quaternary and Younger Faults from the Fault Activity Map of California, version 2.0: California Geological Survey ([http://www.consrv.ca.gov/CGS/information/publications/QuaternaryFaults\\_ver2.htm](http://www.consrv.ca.gov/CGS/information/publications/QuaternaryFaults_ver2.htm)).
- Carnec, C., and H. Fabriol, 1999. Monitoring and modeling land subsidence at the Cerro Prieto geothermal field, Baja California, Mexico, using SAR interferometry, *J. Res. Lett.* 26, p. 1211–1214.
- Eneva, M., G. Falorni, D. Adams, J. Allievi, and F. Novali, 2009. Application of satellite interferometry to the detection of surface deformation in the Salton Sea geothermal field, California, *Geothermal Resources Council Transactions* 33, p. 315–319.
- Fay, N. P., and E. D. Humphreys, 2005. Fault slip rates, effects of elastic heterogeneity on geodetic data, and the strength of the lower crust in the Salton Trough region, southern California, *J. Geophys. Res.* 110, B09401, doi:10.1029/2004JB003548.
- Ferretti, A., C. Prati, and F. Rocca, 2000. Nonlinear subsidence rate estimation using permanent scatterers in differential SAR Interferometry, *IEEE Trans. Geosc. Rem. Sensing* 38, p. 2202–2212.
- Ferretti, A., G. Savio, R. Barzaghi, A. Borghi, S. Musazzi, F. Novali, C. Prati, and F. Rocca, 2007. Submillimeter accuracy of InSAR time series: Experimental validation, *IEEE Trans. Geosci. Rem. Sensing* 45, p. 1142–1153.
- Fialko, Y., 2006. Interseismic strain accumulation and the earthquake potential on the southern San Andreas fault system, *Nature* 441, p. 968–971, doi:10.1038.
- Fialko, Y., and M. Simmons, 2000. Deformation and seismicity in the Coso geothermal area, Inyo County, California: Observations and modeling using satellite radar interferometry, *J. Geophys. Res.* 105, p. 21,781–21,793.
- Genrich, J. F., Y. Bock, and R. G. Mason, 1997. Crustal deformation across the Imperial Fault: Results from kinematic GPS surveys and trilateration of a densely-spaced, small-aperture network, *J. Geophys. Res.* 102, p. 4985–5004.
- Hanssen, R.F., 2001. *Radar Interferometry: Data Interpretation and Error Analysis*, Kluwer Acad. Publ., London.
- Hill, D. P., 1977. A model for earthquake swarms, *J. Geophys. Res.* 82, p. 1347–1352.
- Lin, G., P.M. Shearer, and E. Hauksson, 2007. Applying a three-dimensional velocity model, waveform cross correlation, and cluster analysis to locate southern California seismicity from 1981 to 2005, *J. Geophys. Res.*, 112, B12309, doi:10.1029/2007JB004986.
- Lofgren, B.E., 1979. Measured crustal deformation in Imperial Valley, California, in *Proceed. First Symp. Cerro Prieto Geothermal Field, Part I, Geothermics* 8, p. 267–272.
- Lohman, R. B., and J. J. McGuire, 2007. Earthquake swarms driven by aseismic creep in the Salton Trough, California, *J. Geophys. Res.* 112, B04405, doi:10.1029/2006JB004596.
- Lyons, S. N., Y. Bock, and D. T. Sandwell, 2002. Creep along the Imperial Fault, southern California, from GPS measurements, *J. Geophys. Res.* 107(B10), p. 2249, doi:10.1029/2001JB000763.
- Meltzner, A.J., T.K. Rockwell, and L.A. Owen, 2006. Recent and long-term behavior of the Brawley fault zone, Imperial Valley, California: an escalation in slip rate?, *Bull. Seismol. Soc. Am.* 96, p. 2304–2328, doi:10.1785/0120050233.
- Oppliger, G., L. Shevenell, and M. Coolbaugh, 2008. Preliminary site assessment of the Redfield Campus, Reno, NV, USA, *Geothermal Research Council Trans.* 32, p. 163–168.
- Oppliger, G., L. Shevenell, and M. Coolbaugh, 2006. Improved visualization of satellite radar InSAR observed structural controls at producing geothermal fields using modeled horizontal surface displacements, *Geothermal Research Council Trans.* 30.
- Thomas, A. P., and T. K. Rockwell, 1996. A 300- to 500-year history of slip on the Imperial Fault near the U.S.–Mexico border: Missing slip at the Imperial fault bottleneck, *J. Geophys. Res.* 101, p. 5987–5997.
- Wicks, C., W. Thatcher, F. Monastero, and M. Hasting, 2001. Steady-state deformation of the Coso Range, east-central California, inferred from satellite radar interferometry, *J. Geophys. Res.* 106, p. 13,769–13,780.